Passive film formation on the new biocompatible non-equiatomicTi 21 Nb 24 Mo 23 Hf 17 Ta 15 high entropy alloy before and after resting in simulated body fluid

Virginie Roche, Yannick Champion, Ivan A Bataev, Alberto Moreira Jorge Junior

To cite this version:

Virginie Roche, Yannick Champion, Ivan A Bataev, Alberto Moreira Jorge Junior. Passive film formation on the new biocompatible non-equiatomicTi 21 Nb 24 Mo 23 Hf 17 Ta 15 high entropy alloy before and after resting in simulated body fluid. Corrosion Science, 2022, 207, pp.110607. 10.1016/j.corsci.2022.110607 . hal-03823720

HAL Id: hal-03823720
https://hal.science/hal-03823720v1

Submitted on 21 Oct 2022

Passive film formation on the new biocompatible non-equiatomic$Ti_{21}Nb_{24}Mo_{23}Hf_{17}Ta_{15}$ high entropy alloy before and after resting in simulated body fluid

Virginie Roche[a,*,1], Yannick Champion[b], Ivan A. Bataev[c], Alberto Moreira Jorge Junior[a,b,d,**]

[a] *Univ. Grenoble Alpes, Univ. Savoie Mont Blanc, CNRS, Grenoble INP, LEPMI, 38000 Grenoble, France.*
[b] *Univ. Grenoble Alpes, CNRS, Grenoble INP, SIMaP, 38000 Grenoble, France*
[c] *Novosibirsk State Technical University, K. Marx Ave. 20, Novosibirsk 630073, Russia*
[d] *Department of Materials Engineering, Federal University of São Carlos, 13565-905 São Carlos, Brazil*

Keywords:
High entropy alloys
Implant storage simulation
In-body implant simulation
Passive film formation
Electrochemical impedance spectroscopy
Corrosion propertie

The $Ti_{21}Nb_{24}Mo_{23}Hf_{17}Ta_{15}$ biocompatible high entropy alloy (HEA) was analyzed for different air-exposure times before corrosion tests in simulated body fluid (SBF), simulating implant air storage before implantation, presenting tremendous surface passivation capacity. Electrochemical impedance spectroscopy indicates layers thickening during air exposure with a very capacitive behavior. Two-time constant relaxation confirmed the formation of a double layer and oxide one. The equivalent $R_{electrolite}$+ (C_{oxide})+ (R//CPE) circuit model simulated the EIS behavior. Atoxic inert oxides were observed by X-ray photoelectron spectroscopy before and after SBF immersion for seven days, not impairing biocompatibility and producing a stable passive film.

1. Introduction

In the domain of biomedical implants, bones are seen as tissues with specific properties that favor functional rehabilitation through biocompatible implants. In this sense, over the last decades, scientists from materials science and orthopedics are cooperatively striving to achieve progress in implant designs relevant to replacing body parts.

Metallic materials are widely applied to replace hips, missing joints or bone, supporting a damaged bone, or yet dental roots. Ti and its alloys (e.g., Ti-6Al-4 V), stainless steels, and Cr-Co alloys are nowadays the most used conventional biomaterials [1], mainly due to some of their mechanical properties and corrosion resistance [2–7].

Such currently used biomedical devices have satisfactory overall mechanical performance and tend, with few exceptions, to be inert relative to interactions with the body and its different tissues and fluids. However, the actual inertness level is often not enough. The body may still react to the device insertion by developing inflammation, allergic responses, and even necrosis, leading to rejection and imposing the device replacement. Substitution may be required shortly after the first surgery (e.g., inflammatory processes) or in the long term (e.g., stress shielding effect, which leads to bone resorption, and loss of implant fixation).

Toxic elements (e.g., V, Al, Ni, Cu, etc.) present in most currently used biomedical alloys may be dissolved by corrosion or released by friction during long-term implantation. They can be heavily harmful, potentially leading to severe troubles such as Alzheimer's, allergic reactions, and cancer [7–9]. There are also serious concerns regarding the above alloys' elastic moduli that are still much higher than bones (10–30 GPa) [10]. The discrepancy between Young's modulus of implant and bone causes the stress-shielding effect that induces bone resorption and jeopardizes the long-term treatment. Moreover, the implant's elastic modulus positively affects bone cell phenotypic growth and differentiation [11,12].

Since the early 2000s, the last generation of β-titanium alloys for biomedical applications, such as Ti-Nb-Zr-Ta and Ti-Mo-Zr-Fe-based alloys, has been developed to tackle the above shortcomings. Indeed, they presented benefits compared to standard Ti alloys and have been regarded as more appropriate materials for implant applications [13].

However, those are metastable alloys: the β-phase stability depends on the hot working process, and subsequent heat treatments may lead to the precipitation of α-phase, martensite, and harmful embrittling ω-phase. As a result, those phases will also result in relevant properties such as Young's modulus, hardness, and ductility. They may therefore turn out to be even worse than the single β-alloy.

Furthermore, adverse soft tissue reactions to debris particulates released by these alloys became an issue of significant concern [14,15]. Indeed, the FDA already recalled the Ti-12Mo-6Zr-2Fe (TMZF) alloy in 2011 because of the release of unacceptable wear debris levels in the human body [15]. Studies continue to be made to improve the wear resistance of the Ti-35Nb-7Zr-5Ta (TNZT) alloy [14,16].

The above limitations shorten the implant lifetime, requiring unanticipated and even recurrent substitution surgeries. This reduced lifetime is particularly and intrinsically challenging in setting implants in young people who would potentially require more than one replacement surgery during their expected life. Unfortunately, this ensemble of shortcomings seriously hampers the use of the presently employed devices. It is therefore imperative to develop a new age breed of orthopedic devices. They need to be more biocompatible, easily integrate into the body, support osseointegration, and restrict diverse rejection phenomena. In this sense, High Entropy Alloys (HEA) started to be studied as possible implant materials. Indeed, in 2017 the TiNbTaZrMo alloy [17] was proposed to have this functionality.

High Entropy Alloys (HEAs) have attracted vast attention in several fields and applications in recent years. Such alloys consist of five or more main chemical elements [18–24] with concentrations ranging from 5 to 35 at%, affording an unparalleled alloying approach [19,25] to raise the alloy's configurational entropy of mixing [26]. A high configurational entropy usually leads HEAs to form multicomponent single-phase solid solutions having either body-centered cubic (BCC), face-centered cubic (FCC), or hexagonal close-packed (HCP) crystal structures [27], driving them to many impressive and unusual properties. These properties come from different atom sizes that make up the crystals. Each atom is bordered by distinct elements and thus undergoes strains caused by the difference in atom sizes and non-symmetrical binding energies [28,29], leading to high strength and hardness by solid solution strengthening, good wear resistance [30–32], and high-temperature stability [33].

The design of a HEA is mainly grounded on semi-empirical parameters estimation and correlation based on Hume-Rothery rules which weigh atomic size mismatches, electronegativities, and valence electron concentrations (VEC) [34–38].

In this way, Eqs. (S1 to S3) presented in the Supplementary Material were proposed to predict the solid-solution formation ability (Ω), correlate to atomic size mismatches (δ), and predict the crystal structures of HEAs.

From those equations, Yang et al. [35] have stated that when $\Omega > 1$, the Gibbs free energy is more influenced by the entropic term and tends to form a solid solution. Guo et al. [20] found that when $\Omega > 1.1$ and $\delta < 6.6\%$, a single-phase solid solution is stabilized. Finally, Guo et al. [20] showed that when $VEC < 6.87$, there is a trend to form body-centered cubic (BCC) solid solutions, while for $VEC > 8$, one may expect face-centered cubic (FCC) solid solutions.

Besides their previously mentioned outstanding qualities, corrosion properties are also of primary concern in any high-entropy alloy. Most HEAs present a superior corrosion resistance related to their chemical composition and surface structure. Therefore, they should be evaluated early in search of new alloys/systems [39,40], mainly when considering biomaterials. Regarding composition, Ti, Zr, Hf, Nb, Cr, Ni, Mo, Ta, and W show passivity properties. Except for W, Cr, and Ni, all other elements are of biological interest for their non-toxicity, biocompatibility, or inertness [41–47]. Such elements facilitate the formation of stable barrier films having high surface ionic resistivity, thus protecting the surfaces of the implant from corrosive species and minimizing electrochemical reactions [22,48–54]. Furthermore, with no detectable intermetallic compounds, the single solid solution phase forming the HEA prevents pitting corrosion that may occur at phase boundaries due to detrimental composition abrupt variations [52]. However, phase structure and elemental segregation can affect the passive film protectiveness by shifting the phases' nobility, influencing dissolution kinetics [55].

In the present paper, we report on a new high entropy alloy for implant application based on the chemical elements mentioned in the preceding paragraph that favor corrosion properties while being of biological interest. Combining specific chemical elements and the Equations S1 to S3, the non-equiatomic $Ti_{21}Nb_{24}Mo_{23}Hf_{17}Ta_{15}$ high entropy alloy was designed.

Prosthesis materials and devices are usually kept in dry environments before application. Depending on the dry storage duration, the passive film can eventually present distinct structures and properties, mainly in the first days of air exposure before being implanted. This work thus proposes a first exploratory analysis of the new non-equiatomic $Ti_{21}Nb_{24}Mo_{23}Hf_{17}Ta_{15}$ high entropy alloy composed of a single BCC phase intended to be used as a biomedical implant material. The study will focus on the passive film formation during different air exposure times before the material's immersion and corrosion behavior once immersed in simulated body fluid (SBF) solution.

2. Experimental procedure/ methodology

Alloy ingots were prepared by arc melting from pure elements under an Ar atmosphere. The alloy ingot was flipped and cast several times to ensure its homogeneity. A cylindrical billet of about 10 cm long and 10 mm in diameter was obtained by pouring the molten into a water-cooled copper mold coupled to the arc-melter. The samples were cut from this cylinder by wire erosion machining (Electrical Discharge Machine, EDM), producing 1 mm thick discs.

The alloy specimens' surface was polished with abrasive paper up to grit P4000, followed by cleaning in deionized water (Milli-Q®), ethanol, and acetone, and then exposed to air for different periods (0 h (~4 min), 6 h, 24 h, and 360 h). The air exposure period was considered to start just after sample preparation and finish just before immersion in the electrolyte. On average, the relative humidity was 50%, and the temperature was 25 °C.

Microstructural characterization and elemental mapping were carried out using the FEG ZEISS Ultra 55 scanning electron microscope (SEM) coupled with X-ray microanalysis (EDS) system with an SDD detector (BRUKER AXS-30 mm^2). EDS mapping was performed using an acceleration voltage of 15 kV and a work distance of 8 mm. Morphological images were taken using an in-lens secondary electron detector (SE) using an acceleration voltage of 3 kV and a work distance of 3 mm to have a high spatial resolution.

The structure was analyzed by X-ray diffraction (XRD) using the PANalytical X′ Pert PRO MPD diffractometer with Cu-Kα wavelength. Data acquisition was performed in the range of 20–100° 2θ angles, in steps of 0.026°, using a speed of 0.25 Hz and an acquisition time of 1000 s per step, using a voltage of 45 kV and a current of 40 mA.

The sample elastic modulus was determined using the free decay elastometer SONELASTIC® from ATCP Physical Engineering.

Hardness measurements were conducted using a microhardness tester (Shimadzu HMV-G 0.205 T), and a Vickers indenter was employed with a load of 500 g.

The corrosion test of the $Ti_{21}Nb_{24}Mo_{23}Hf_{17}Ta_{15}$ HEA was conducted in an SBF solution (for ions concentrations, please refer to Table S1 in the Supplementary Material) at 37 °C and in the dark. The electrochemical measurements were carried out in a three-electrode cell with a platinum mesh as a counter electrode and saturated calomel electrode (SCE) as reference using a Gamry Ref 600 + potentiostat. The working electrode surface area of 0.3 cm^2 was exposed to the electrolyte for electrochemical measurements, and the counter electrode area was 4 cm^2. First, the sample/working electrode is immersed in SBF solution for 7200 s to stabilize the open-circuit potential (OCP). Electrochemical impedance spectroscopy (EIS) measurements were carried out around

OCP after two hours of immersion, which was enough for surface

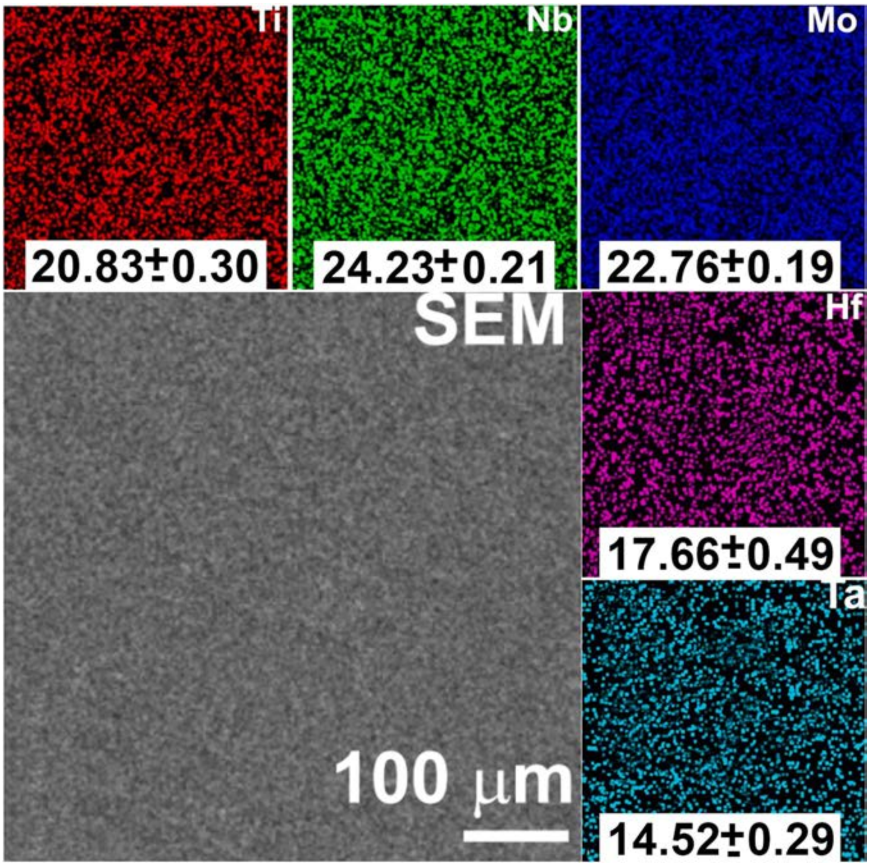

Fig. 1. Elemental mapping of the $Ti_{21}Nb_{24}Mo_{23}Hf_{17}Ta_{15}$ HEA. SE imaging of the surface area used to perform the EDS analysis; distribution and atomic % composition of the different alloy elements: Ti, Nb, Mo, Hf, and Ta, from the top left to the bottom right positions of the SEM image, respectively.

stabilization; the voltage amplitude was 10 mV, and the frequency range was between 10^{-2} to 10^{5} Hz. A second 600 s resting was done to stabilize the OCP, and thus, potentiodynamic polarization was conducted in a range from − 0.03 V to + 2.0 V vs. OCP, and the scan rate was 1 mV/s. The software Biologic EC-Lab V10.40 was used for data fitting and analysis.

X-ray photoelectron spectroscopy (XPS) was carried out using the THERMO SCIENTIFIC K-ALPHA X-ray photoelectron spectrometer, using an Al-Kα micro-focused monochromator, and a spot size of 400 μm. Ten scans were carried out at a 90° beam angle for each element, and the survey spectra were recorded in binding energy (BE) range from 0 to 1100 eV using a step of 0.10 eV. The BE scale was calibrated using the C1s peak at 285 eV. The Avantage 4.88 software was used to analyze XPS data, where peaks were fitted employing the Smart baseline subtraction.

3. Results and discussion

3.1. Alloy characterization

3.1.1. Chemical composition and elemental distribution after melting

Fig. 1 depicts the EDS analysis of a large surface area (ca 500 × 500 μm, cf Fig. 1a). Fair distributions are shown in the elemental mapping pictured in the small Figures around the SEM image for Ti, Nb, Mo, Hf,

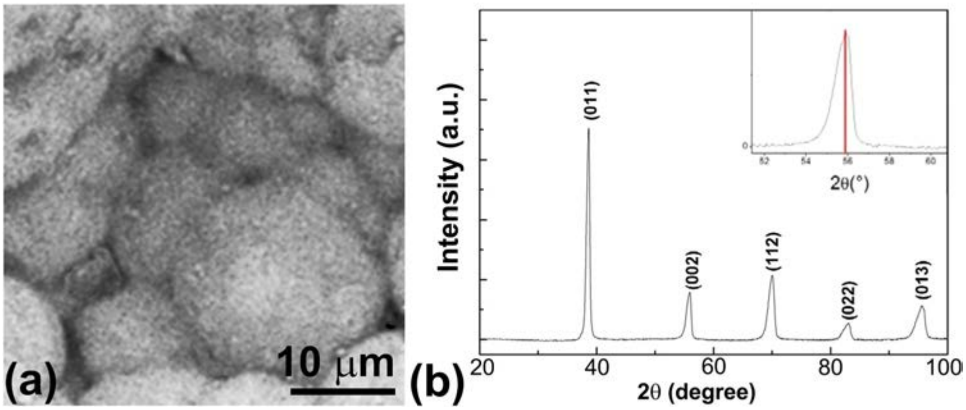

Fig. 2. (a) SE-SEM image of as-cast $Ti_{21}Nb_{24}Mo_{23}Hf_{17}Ta_{15}$ high entropy alloy. (b) XRD pattern for $Ti_{21}Nb_{24}Mo_{23}Hf_{17}Ta_{15}$ HEA. The inset of Fig. 2b highlights the (002) peak as an example.

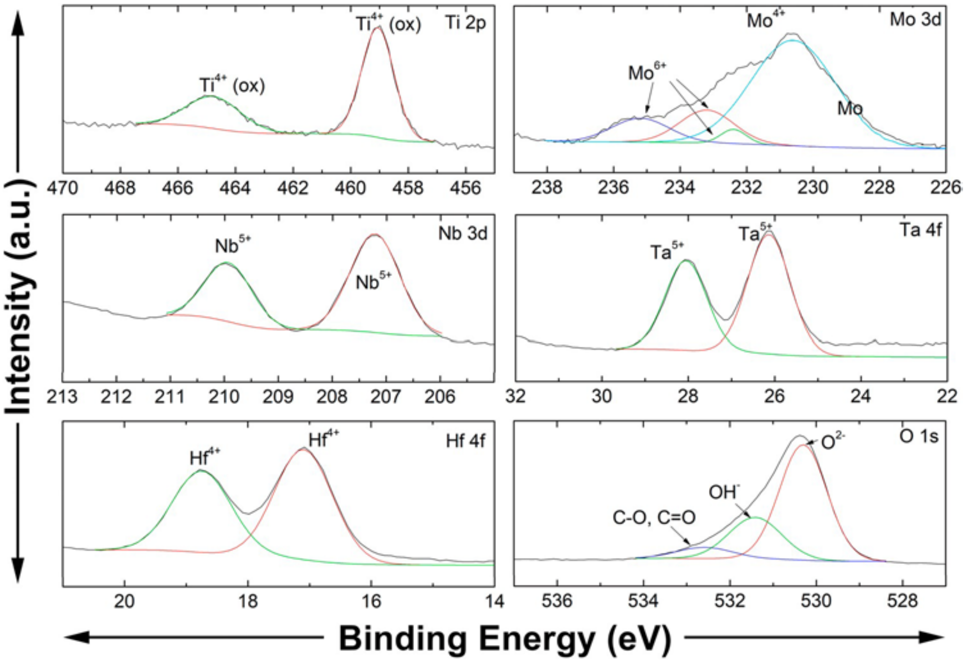

Fig. 3. High-resolution XPS spectra of Ti2p, Mo3d, Nb3d, Ta4f, Hf4f, and O1s peaks obtained for the air-exposed surface for 24 h before immersion in SBF solution and electrochemical test.

and Ta, from the top left to the bottom right positions, respectively. Such elemental mapping confirms their homogeneous distribution. The elemental composition measured by EDS is given at the bottom of each small Figure for the different elements, indicating a similar concentration of the nominal values of the $Ti_{21}Nb_{24}Mo_{23}Hf_{17}Ta_{15}$ HEA.

3.1.2. Microstructural and Structural characterization (Crystallography)

Fig. 2a presents a SE-SEM image of the as-cast $Ti_{21}Nb_{24}Mo_{23}Hf_{17}Ta_{15}$ HEA, revealing a microstructure characterized by equiaxed grains with an average size of 11 ± 3 μm. The XRD pattern given in Fig. 2b shows diffracted peaks related to crystalline planes of a typical BCC structure ((110), (200), (211), (220), and (310)). No other peaks related to any intermetallic phases were detected. The calculated lattice parameter is 3.2980 Å, close to the theoretical value (3.4041 Å) and those of other high entropy alloys [56]. The theoretical value was calculated using the atomic radii average of elements and applying the classical equation for the BCC structure $a = 4R/\sqrt{3}$, where $\mathbf{a}$ is the lattice parameter, and $\boldsymbol{R}$ is the atomic radius.

The results presented in Figs. 1 and 2 constitute strong evidence that a non-equiatomic solid solution was formed solely based on five refractory elements recognized for their biocompatibility and the generation of atoxic surface oxides for the human body. Indeed, the XRD spectrum yields asymmetrical peaks' profiles as illustrated by the inset Fig. 2b: regarding the peak maximum, the left side is clearly broader than the right one. Consistently with the high entropy alloys' nature, this peak asymmetry might indicate a lattice parameter gradient. Since the HEA's main characteristics are different and non-ordered elements occupying the atomic sites, the lattice parameter may locally vary according to the neighboring atoms, producing several similar BCC phases as also observed in [57].

3.2. Some mechanical properties

Although not an objective of the present manuscript, some mechanical properties related to stress-shielding and debris release are of uttermost importance for the reliability of any implant in-service conditions; therefore, Young's modulus, E, and the Vickers microhardness, HV, have been straightforwardly measured as described in the methodology section. The obtained values were 90 ± 5 GPa for Young's modulus and 453 ± 10 for the HV.

The mechanical properties of the new $Ti_{21}Nb_{24}Mo_{23}Hf_{17}Ta_{15}$ HEA compared to Ti and Ti-alloys and some other conventional materials used for implants as well as the bone itself are given in the Supplementary Material (Table S2). The new $Ti_{21}Nb_{24}Mo_{23}Hf_{17}Ta_{15}$ HEA shows an attractive and promising combination of mechanical properties that should allow its use as hard tissue substitution implants such as hip and knee prostheses [5,7]. Indeed, compared to most of the other alloys, the new $Ti_{21}Nb_{24}Mo_{23}Hf_{17}Ta_{15}$ HEA presents lower Young's modulus (potentially reducing stress shielding effects), higher hardness (lower tendency to debris release), and higher tensile strength (allowing optimized shaping of smaller and lighter implants).

3.3. Surface properties: electrochemical responses and film formation

Surface characterization by XPS was used to comprehensively assess chemical bonds formed on air-exposed for 24 h sample before immersion in SBF solution and electrochemical test, simulating dry implant storage before implantation. High-resolution spectra are presented in Fig. 3. The NIST XPS standard [58] was used to determine elements' binding energies.

The XPS analysis revealed strong Ti2p, Mo3d, Nb3d, Ta4f, Hf4f, and O1s peaks. The fitting of the Ti2p spectrum demonstrated the presence of only Ti^{4+} (459.08 eV and 464.88 eV), corresponding to TiO_2. The Mo3d spectrum gave peaks of Mo^{4+} (227.48 eV and 230.58 eV) and Mo^{6+} (232.38 eV, 233.18 eV, and 235.28 eV), matching MoO_2 and MoO_3, respectively. Like in the Ti2p spectrum, the fitting of Nb3d, Ta4f, and Hf4f spectra gave only one oxidized state for each one of them, referring to the peaks of Nb^{5+} (207.18 eV and 209.98 eV), Ta^{5+} (26.12 eV and 28.08 eV), and Hf^{4+} (17.08 eV and 18.78 eV), correspondent to the oxides Nb_2O_5, Ta_2O, and HfO_2, respectively. The O1s spectrum can be split into three peaks, O^{2-} (529.90 eV), OH^- (530.57 eV), which probably overlaps a peak of some water (532.23 eV) from air-humidity, and carbon-oxygen bonds (C-O and C=O, 532.78 eV) from some hydrocarbon surface contamination.

The cationic concentrations in the surface film were calculated on the area under the main peak divided by an atomic sensitivity factor

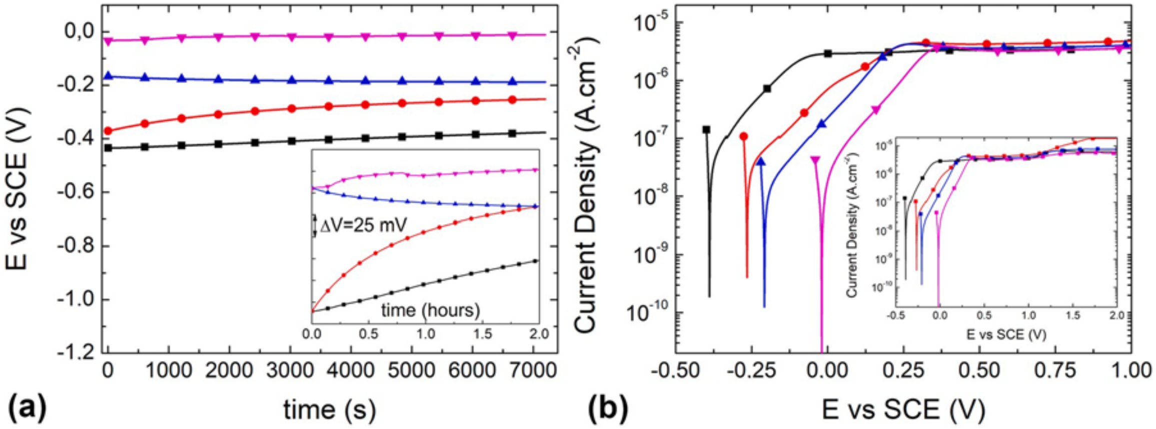

Fig. 4. (a) open-circuit potential (OCP) measurements. **Inset:** presents polarization curves up to + 2.0 V. (b) polarization curves of $Ti_{21}Nb_{24}Mo_{23}Hf_{17}Ta_{15}$ HEA after different times of air storage before immersion in SBF solution at 37 ° C in the dark: (■) 0, (●) 6, (▲) 24, and (▼) 360 h. **Inset:** Open-circuit potential evolution after two hours of immersion in SBF plotted in arbitrary scale within a 200 mV range (zoomed-in), illustrating the potential drift better. The last points in the curves correspond to the OCP conditions in which the polarization curves have been measured.

(ASF). These calculations gave the values of 31% for Mo-oxides (MoO_2 and MoO_3), followed by 24% of Nb_2O_5. The approximately same amount of 15% was found for the other oxides (TiO_2, Ta_2O, and HfO_2).

Indeed, once the sample was simply left in the air for only 24 h, these results show that this alloy has an astonishing capacity for oxidation. Hence, there is a passive film formation, leading to enhanced surface stability and, consequently, ennobling the OCP behavior, as will be discussed further. Also, besides biological interest due to their non-toxicity, biocompatibility, or inertness [41–47], the alloying elements present in the HEA produced only non-toxic and inert oxides. Therefore, such oxides will not harm biocompatibility and may produce a stable passive film to protect the sample surface against corrosion in the body fluid.

Fig. 4 depicts the results of open-circuit potential (OCP) measurements and the polarization curves of the specimens after different air exposure times, from 0 to 360 h, i.e., immediately after sample preparation until after 15 days. The open-circuit potential (Fig. 4a) of samples immersed in SBF solution stabilized after two hours. It significantly increased with the air-exposure time, from ca − 380 mVsce for fresh samples to ca − 10 mVsce after 15 days. The OCP evolution during two hours of immersion, before the polarization curves were acquired, was much more stable after several days of storage under air-exposure conditions, as illustrated in the inset of Fig. 4a. The potential evolution was more pronounced in the freshly exposed specimen — an almost linear drift — than in longer exposure times. Such results confirm the above observations regarding passive film formation and stability once the freshly exposed sample already showed a good value for open-circuit potential, which grew with the air-exposure time. Those are expected results when the material rests in a solution where the passive film tends to run thicker and more homogeneous with time, meaning nobler behavior and, thus, higher and more stable open-circuit potentials. However, one must stress that the passive film was formed in an air environment with very low humidity (please refer to XPS analysis in Fig.3), confirming the studied alloy's oxidation capacity. Another direct consequence of the film evolution is that the corrosion current (Fig. 4b) slightly decreased by less than one decade as the storage time increased, notwithstanding the first value obtained for the freshly prepared and immersed sample, which is already very low, < 0.1 μA cm-2.

Despite the differences in the OCP values and evolution, the polarization curves are very similar regardless of the exposure time. All

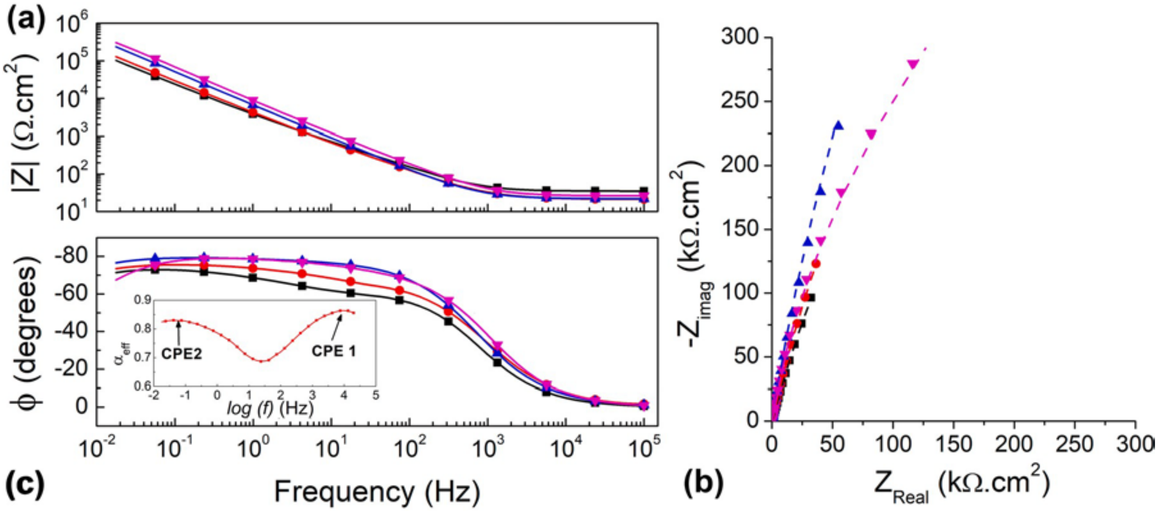

Fig. 5. Electrochemical impedance spectroscopy analysis of $Ti_{21}Nb_{24}Mo_{23}Hf_{17}Ta_{15}$ HEA after different times of air storage before immersion in SBF solution at 37 ° C in the dark: (●) 0, (•) 6, (▲) 24, and (▼) 360 h. (a) Bode moduli plots; (b) Nyquist plots, where the dashed lines represent fittings' results; (c) Bode phase plots (Φ = phase angle); **inset:** time-dependency of the CPE element, α_{eff}, illustrating the two-time constant relaxation associated with CPE 1 and 2 in the case of the 6-hour aged specimen.

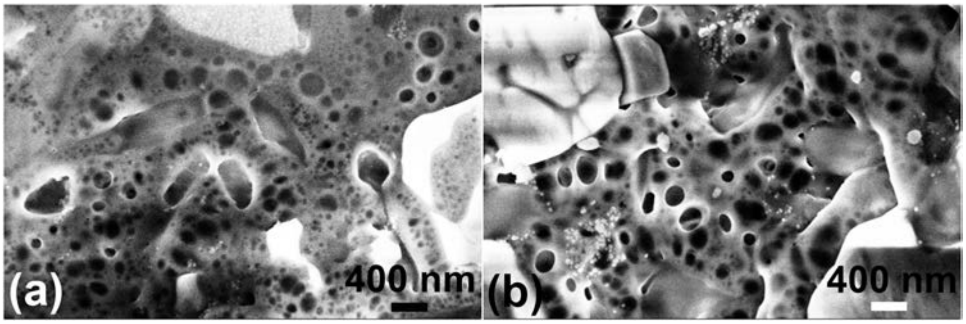

Fig. 6. SEM analysis presenting surface images of samples previously exposed to the air for 24 h in (a) and 360 h in (b), showing the surface oxide film after corrosion tests in the SBF solution, both in the dark at 37 ° C.

samples clearly showed a passive behavior after an active first part close to the corrosion potential: the current densities reached a stable and wide-ranging plateau with passivation currents converging to a narrow range between ca 3 and 5 μA cm^{-2}. The slight increase in current observed above approximately + 1.0 V (inset of Fig. 4**b**) refers to the oxidation of the water. The low values of the current densities plateau are due to restrained mass transport through the oxide layer [59]. The film seems to be already protective at the very early stages of formation, observed by the absence of an active region in which the current density is higher than the passivation plateau current density, as may be the case with stainless steels in acidic media. Therefore, The corrosion current density (j_{corr}) will be considered as the current density of the passivation plateau (j_{pass}), as in [59,60].

The fact that even the sample immersed just after being polished already showed a passive behavior with roughly the same passivation current densities of aged ones is a first indication of the highly passive characteristic of the $Ti_{21}Nb_{24}Mo_{23}Hf_{17}Ta_{15}$ HEA. Indeed, this fact demonstrates a natural tendency of the recovery capacity of protection in the case of passive film remotion during implantation. In a straightforward comparison with other materials widely used in biomedical applications, the j_{pass} values shown in Fig. 4 are smaller than for pure titanium (ca 11 μA cm^{-2}) [61] and similar to those for the Ti-6Al-4 V alloy (3.4 μA cm^{-2}) [62].

The absence of pitting corrosion inferred from Fig. 4 and microscopic observations is also very positive. Indeed, the high-current density values associated with those localized attacks may source the undesired release of metallic cations and debris.

The synergetic combination of oxides (Fig. 3) may be responsible for this excellent corrosion behavior. Indeed, as observed in the current literature [63–82], TiO_2 and Nb_2O_5 are recognized as being very stable and corrosion-resistant oxides. Furthermore, Nb^{5+} cations enhance the TiO_2 passivation capacity. MoO_2 and metallic Mo on the substrate surface might be the main factor in improving the corrosion resistance of Mo-alloyed stainless steels due to the formation of the molybdenum passive film [69]. MoO_3 has even a more protective behavior against aggressive Cl^- ions by avoiding pitting or facilitating its repassivation [73]. Hf is one of the most corrosion-resistant metals and can protect and control corrosion rates [74,75]. Finally, Ta_2O_5 is the most stable oxide in the present HEA, improving the formed film's overall passivation capacity [79–82].

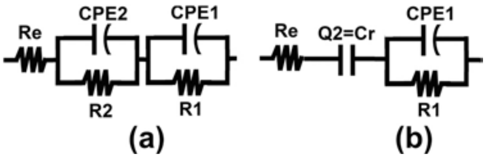

Fig. 7. Electrical equivalent circuits (EEC) for fitting the EIS results related to the observed two-layered structure. (a) the complete circuit used for initial simulations. (b) the final circuit used after preliminary analyses, considering $R2 \rightarrow \infty$. The pair (CPE_1, R_1) represents the double layer CPE and its charge transfer resistance. The pair (CPE_2, R_2) represents the CPE and charge transfer resistance of the thick oxide layer. Q2 is the constant phase element, and as discussed further, Cr is the capacitance obtained using "Cole-Cole" diagrams [93,94].

One of the crucial aspects of medical implant applications is how the material's surface interacts with the physiological electrolyte at the interface level. Therefore, a deeper analysis of the $Ti_{21}Nb_{24}Mo_{23}Hf_{17}Ta_{15}$ HEA behavior was performed through electrochemical impedance spectroscopy. Fig. 5 summarizes the results obtained from the EIS in the SBF solution at 37 ° C in the dark after different times of air storage. Like the polarization results, the impedance diagrams showed similar behavior for the different exposure times. The Bode moduli (Fig. 5a) increase with the frequency decreasing, suggesting an increase in corrosion resistance at the lowest frequencies. Also, the Bode moduli show a straight-line increase as the frequency decreases to 10 mHz without any low-frequency plateau. The absence of low-frequency saturation of the impedance modulus is typical of highly capacitive behaviors, like those of high-protective passive films [83]. As seen in the Nyquist representation (Fig. 5b), this response is characterized by truncated capacitive plots that can be assimilated to near-straight lines close to the vertical axis. This behavior is yet a non-ideal behavior better described by a non-ideal capacitance, a constant-phase element, CPE, built-up from a frequency distribution due to a charge transfer mecha- nism on an inhomogeneous surface [56,84,85].

The Bode phase plots in Fig. 5**c** effectively depict frequency distributions supporting a CPE behavior. Indeed, instead of a narrow wave of the phase-angle variation with frequency, all the diagrams show a stretched, not well-defined, phase relaxation. This phase profile is typical of entangled relaxation frequencies — the frequency distribution — originated from multiple (strictly speaking, more than one) time constants.

The number of time-constants determination, and thus, the number of intervening processes at the interface, is a difficult task. A practical approach is based upon the analysis of the frequency evolution of the CPE parameter α — which quantifies the deviation from an ideal capacitance — through Eq. (4) [86], yielding the frequency-dependent CPE parameter α_{eff}:

$$\alpha_{eff}(f) = -\frac{d\log\left|Z_{imag}(f)\right|}{d\log f} \tag{4}$$

Since Eq. (4) utilizes the derivative of the impedance imaginary part ($\boldsymbol{Z}_{imag}$) in log-log space, the resulting α_{eff} is more responsive than the phase angle and is more prone to capture changes in the CPE behavior. Such sensitivity is illustrated in the inset in the Bode phase plot in Fig. 5c, taking the 6-hour aged specimen as an example. The inset shows an unambiguous double relaxation indicating the presence of two CPEs reflecting the existence of two relaxations. The existence of two-time constants can be assimilated to a staggering surface structure corresponding to the presence of two layers of surface oxides. The SEM

Table 1

- Measured values of Cr obtained from the "Cole-Cole" diagrams presented in Fig. S1 in the Supplementary Material and Electrolyte resistance (Re) from the analysis.

Sample	Cr (μF.cm^{-2})	Electrolyte resistance (Ω.cm^2)
0 h	5.32 ± 2.31	35.12 ± 0.02
6 h	4.38 ± 0.20	20.70 ± 0.11
24 h	3.75 ± 0.15	22.00 ± 0.03
360 h	4.04 ± 0.23	26.51 ± 0.02

Table 2

- Electrical parameters obtained by fitting the experimental impedance data to the equivalent circuit, using the software Biologic EC-Lab V10.40, for air-exposed samples after corrosion tests at 37 ◦C in the SBF solution.

Sample	CPE$_1$ (Ω^{-1}.cm^{-2}s$^{\alpha}$)	α_1	R$_1$ (Ω.cm^2)	α_2	R^2 (%)
0 h	20.0×10^{-6}	0.81	3.00×10^5	0.80	99.84
6 h	19.6×10^{-6}	0.82	3.57×10^5	0.89	99.90
24 h	15.4×10^{-6}	0.88	$4,69 \times 10^5$	0.86	99.81
360 h	14.6×10^{-6}	0.88	7.04×10^5	0.89	100.00

analysis in Fig. 6 gives samples' images after 24 h and 360 h under air-storage conditions showing a surface oxide layer after corrosion tests in the SBF solution. From these images, one may observe a porous and full of defects thick oxide surface has grown on the substrate. Such oxide configuration may be of high capacitance, as discussed above (Fig. 5), and very high ohmic resistance, which will be determined further. Different authors [87–92] reported this two-layer structure for conventional Ti alloys with similar elements.

This two-layered structure can be assimilated to a two-stage electrical equivalent circuit (EEC) like the one depicted in the inset of Fig. 7**a**. In this equivalent circuit, R_e represents the electrolyte resistance (the high-frequency limit of the impedance), the pair (CPE$_1$, R$_1$) represents the double layer CPE and its charge transfer. The pair (CPE$_2$, R$_2$) represents the CPE and charge transfer resistance of the thick oxide layer.

In a first fitting attempt using the software Biologic EC-Lab V10.40, we verified that values of R2 were very high (in order of magnitude of 10^{10}), which grew with the air-exposition time during the first 24 h, indicating thickening of the oxide layer. In this situation, R2//Z$_{\text{CPE2}}$ always gives Z$_{\text{CPE2}}$ for any frequency. Therefore, we decided to exclude R2, considering it an open circuit. However, this procedure did not allow us to use the Hsu and Mansfeld method [95] to calculate the oxide capacitance. Hence, we used the "Cole-Cole" diagram to estimate the total capacitance, as suggested in [93,94], and verify the nature of such a determining capacitance.

The graphs of the "Cole-Cole" diagram express the complex capacitance as a function of the variation of capacitance's imaginary part (Cimg) with respect to the real part (Cr). The real part is represented by Eq. (5) and the imaginary part by Eq. (6).

$$C_r = \frac{-Zimg}{2\pi f x \left(Zimg^2 + Zr^2_{\text{corrected by Re}}\right)} \qquad (5)$$

$$-C_{img} = \frac{Zr_{\text{corrected by Re}}}{2\pi f x \left(Zimg^2 + Zr^2_{\text{corrected by Re}}\right)} \qquad (6)$$

where Zr and Zimg are the impedance real and imaginary parts, respectively, both given in Ω.cm^2.

Graphs of "Cole-Cole" diagrams obtained from one of the data sets for air-exposed samples are presented in Fig. S1 in the Supplementary Material. Measured values are given in Table 1**.**

The Cole-Cole corresponds to the capacitance at infinite frequencies. Consequently, considering the EEC in Fig. 7a, finally, it will give the sum of 1/C1 + 1/C2, being C1 relative to CPE1 and C2 to CPE2. As suggested in [94], a double layer capacitance is expected to be larger than 30 μF. cm^{-2} and taking into account the obtained values for Cr, such a sum will give the value of 1/C2 because Cr values are much smaller than Cdl. Therefore, by neglecting the double layer capacitance, one may infer that the obtained values for Cr are directly related to C2, which is, as supposed above, an oxide capacitance related to CPE2.

After this preliminary analysis, the EEC presented in Fig. 7b was used to fit the EIS data for all the analyzed conditions. A phase element impedance is $Z_{CPE} = [Q(j\omega)^{\alpha}]^{-1}$. α is defined above, Q is the constant phase element, and ω is the angular frequency. Re was determined using "Cole-Cole" and bearing in mind that Q2 was set to be Cr (both in Table 1), R1 and CPE1 values, received by fitting the experimental data to the EEC and α_1 and α_2, used for the fitting (Eq. 4 and Fig. 5c), are given in Table 2. The coefficient of determination (R^2) values, which indicate the goodness of fitting of a model, are close to 100%, indicating the excellent agreement between experimental and theoretical data. Such an agreement can also be verified in dashed lines in Fig. 5b, graphically representing the good obtained fitting. The α values close to 0.9 indicate that the respective layer behavior gets closer to that of an ideal capacitor, which is immersion-time independent [96].

The electrolyte resistance is characterized by Re (Tables 1 and 2), whose values are in the magnitude order of 20–30 Ω.cm^2, i.e., an environment with high conductivity.

Pores' resistances are represented by R1, which are of high values and increase with the air-exposure time, indicating porosity decreasing and oxide film densification. Indeed, Fig. 6 confirms this hypothesis. In other words, as one may observe in Fig. 6, the porous surface is initially formed by extensive defects (not round shaped, from 0.6 to 1.2 μm in length) and pores (round ones) whose sizes range from 30 to 350 nm. As time passes, the oxide film becomes more compact (smaller number of pores) and homogeneous, defects disappear, and smaller pores are consumed by the oxides forming the film. Finally, only large pores of around 240 nm in diameter are visible.

However, those R1 values are more than four orders of magnitude smaller than the previously calculated R2, supporting the removal of R2 from the circuit. Indeed, the large values for R2, related to the oxide film, support the high corrosion resistance and indicate its good passivating/protective behavior in the SBF solution. Also, it indicates that the corrosion resistance is virtually exclusive to this oxide layer, as observed in titanium alloys used for implant application [97–99].

Effective capacitances for the double layer (Cdl) can be calculated using the values of CPE$_1$ (Q$_1$ and α_1), Re and R$_1$ reported in Tables 1 and 2 using Brug's equation [100] (Eq. (7)). Effective capacitance values (C$_{\text{eff}}$ - C$_{\text{dl,}}$ and Cr) can be associated with the film thickness using Eq. (8), which is valid for a parallel-plate capacitor model of a homogeneous oxide layer:

$$C_{eff1} = C_{dl} = Q_1^{1/\alpha}\left(R_e^{-1} + R_1^{-1}\right)^{(\alpha_1-1)/\alpha_1} \qquad (7)$$

*

$$d = \frac{\varepsilon_r\varepsilon_0}{C_{eff}} \qquad (8)$$

where ε_0 is the vacuum permittivity (8.85 × 10–14 F. cm^{-1}), and ε_r is the material relative dielectric constant.

Even having an approximate amount of oxides, reliable relative dielectric constants are challenging to find in the literature. For example, values of the relative dielectric constant for TiO2 can be found from 40 to 145 [101–104]. Also, because of the difference between oxides amounts, one cannot be sure if they are homogeneously distributed. Using XPS data, several equations exist to calculate the oxide layer thickness (for instance, in [105,106]). However, invariable, all of them need a metallic peak to get the results, and some of them are impossible to be used with the incidence angle used in this work. Considering these facts, we considered a value of 50 for the material's relative dielectric constant as a good value to have an approximate film thickness.

Table 3

Double layer capacitances calculated using fitting values in Table 2, oxide film capacitance (Cr) taken from Table 1, and thicknesses of the double layer and oxide film, for the different air-exposition periods.

Sample	Cdl (μF.cm^{-2})	Thickness$_{Cdl}$ (nm)	Cr (μF.cm^{-2})	Thickness$_{Cr}$ (nm)
0 h	92.69	0.48	5.32	8.32
6 h	73.36	0.60	4.38	10.10
24 h	34.28	1.29	3.75	11.80
360 h	33.13	1.34	4.04	10.95

Therefore, the double layer capacitances calculated using fitting values in Table 2 for the different air-exposition periods and thicknesses of the double layer and oxide film, using $\varepsilon_r = 50$, are presented in Table 3.

The values reported in Table 3 for Cdl and their thicknesses agree with double-layer capacitances [94]. Cdl and Cr capacitance values decrease with air-exposure times up to 24 h, which becomes constant. Such a decrease corroborates with thickness values that reached a maximum at 24 h that were held for longer times. This behavior may also correlate to decreasing porosity and oxide film densification, as observed above for R1 and justified using Fig. 6.

The thickness values obtained for the oxide layer may be confirmed by the XPS results presented in Fig. 3**.** In other words, bearing in mind that no metallic peaks were detected means that the thickness is larger than the expected maximum depth of information (between 5 and 7 nm [107]), ensuring the values presented in Table 3. Therefore, inside this scenario, one may only affirm that the oxide film thickness massively grows with air exposure and is at least more extensive than 5 nm, even with the above considerations regarding the relative dielectric constant. It is noteworthy that this thickness was inferred from the XPS results presented in Fig. 3 and was acquired after air exposure for only 24 h without immersion in the SBF solution, demonstrating the high oxidation capacity of this HEA again.

XPS results presented in Fig. 3 show that alloying elements in the HEA exposed to the air for 24 h, simulating dry implant storage before implantation, resulted in only atoxic and inert oxides that produced a well passivated HEA surface. However, one may ask about the consequences of long-term exposition to body fluid. XPS was used to characterize the air-exposed surface for 24 h sample after immersion in SBF solution at 37 °C and the dark for seven days, simulating in-body implant conditions. High-resolution spectra are presented in Fig. 8, whose elements' binding energies were determined by the NIST XPS standard [58]. These XPS spectra show no chemical differences between air-exposed and air-exposed and immersed in SBF.

Calculations showed that the cationic concentration of HfO_2 increased by 7% and Ta_2O by 2%. Consequently, concentrations of other oxides decreased by almost 3%. Considering errors related to measurements and calculations, one may consider that only HfO_2 had a not-so-significant change. Therefore, after implantation, the surface continues to have the same excellent characteristics as during air storage or even improving corrosion resistance a bit because, as stated before, HfO_2 improves the formed film's overall passivation capacity. Finally, after implantation, the alloying elements present in the HEA will produce only non-toxic and inert oxides that will not impair the biocompatibility and produce a stable passive film to protect the sample surface against corrosion in the body fluid.

4. Summary and conclusions

This work presented a first exploratory analysis of the new $Ti_{21}Nb_{24}Mo_{23}Hf_{17}Ta_{15}$ high entropy alloy composed of a single BCC phase intended to be used as a biomedical implant material. Prosthesis materials and devices are usually kept in dry environments before implantation. Therefore, implant storage simulation was performed by a study focused on the passive film formation during different air exposure times before the material's immersion and corrosion behavior when

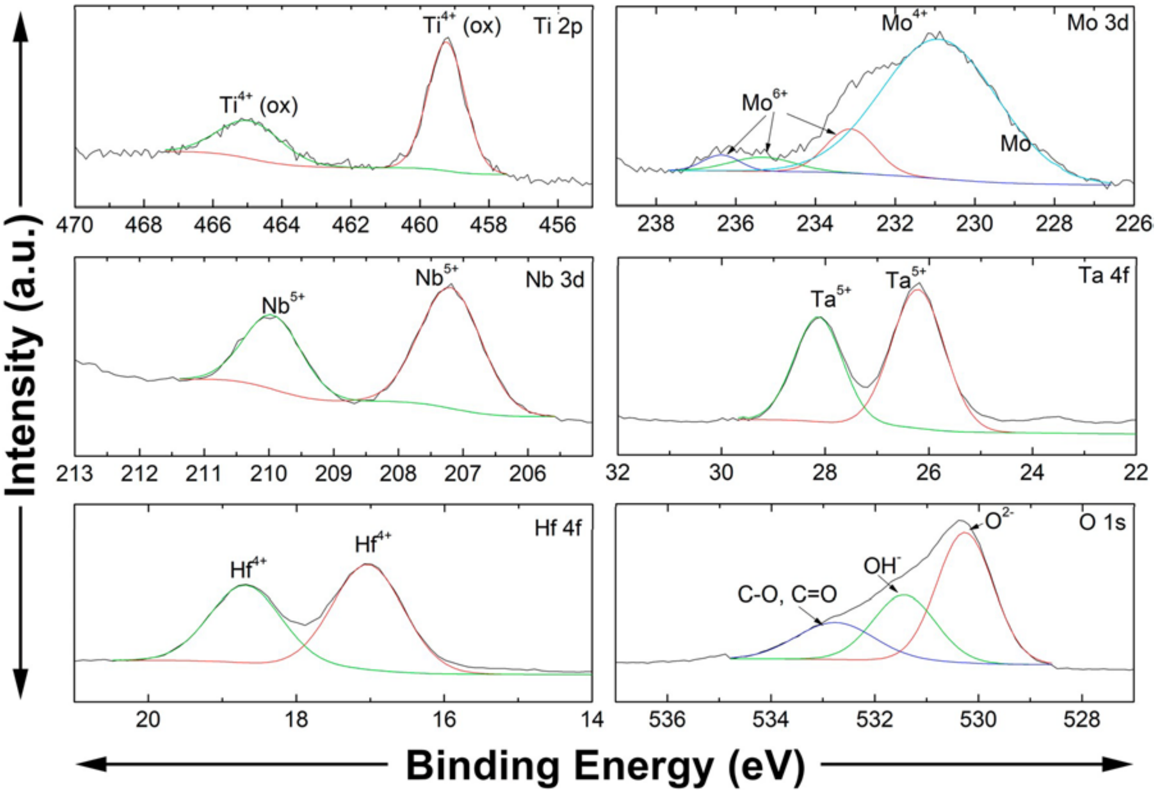

Fig. 8. High-resolution XPS spectra of Ti2p, Mo3d, Nb3d, Ta4f, Hf4f, and O1s peaks obtained for the air-exposed surface for 24 h sample after immersion in SBF solution at 37 °C and the dark for seven days, simulating in-body implant conditions.

immersed in simulated body fluid (SBF) solution. Samples were polished and air-exposure times before immersion varied from 0 h to 360 h. In-body passive film formation after implantation was simulated by resting the alloy for seven days in SBF solution. The conclusions are summarized in the following paragraphs:

This HEA presented a tremendous capacity for surface passivation. The stable passive film produced a very corrosion-resistant surface.

OCP values significantly increased with the air-exposure time and showed fast stabilization and indicated that the film forms very fast once the freshly exposed sample already showed a good value for open-circuit potential, which grew with the air-exposure time. The surface nobless, indicated by the increase in OCP values, improved with the air-exposure time.

The current densities reached a stable and wide-ranging plateau with low values of the current densities, inferred to be due to restrained mass transport through the oxide layer.

Electrochemical impedance spectroscopy (EIS) indicates double and oxide layers thickening during air exposure up to 24 h, becoming constant. EIS modulus increased a lot and presented a very capacitive behavior. The continuous increase of the impedance modulus in these samples suggested that the corrosion resistance enhanced with the air-exposition time.

The presence of a double layer and a thick porous one was confirmed by scanning electron microscopy (SEM) and by two-time constant relaxation, indicating two CPEs. The equivalent $R_{electrolite}$+ (C_{oxide})+ (R//CPE) circuit efficiently simulated the EIS behavior. Simulations corroborated the above conclusions regarding potentiodynamic polarization results by revealing a capacitive behavior, corroborating the protective response of the surfaces.

XPS results showed that the passive film formed after air exposition (simulating implant storage) and after stimulation of the implant in-body is composed of chemical-stable oxides of the five alloy elements. No free metallic ions were found, as confirmed by XPS analyses of samples guaranteeing the device's inertness after implantation and not impairing biocompatibility.

CRediT authorship contribution statement

Alberto Moreira Jorge Junior: Conceptualization, Methodology, Investigation, Formal analysis, Resources, Writing – review & editing. **Ivan A. Bataev:** Validation, Formal analysis, Writing – review & editing. **Yannick Champion:** Conceptualization, Methodology, Resources, Writing – review & editing. **Virginie Roche:** Conceptualization, Methodology, Resources, Writing – review & editing.

Declaration of Competing Interest

The authors declare that they have no known competing financial interests or personal relationships that could have appeared to influence the work reported in this paper.

Data Availability

The raw/processed data required to reproduce these findings cannot be shared at this time as the data also forms part of an ongoing study. Some data can be made available upon request.

Acknowledgments

A.M.J.J acknowledges the Sa˜ o Paulo Research Foundation - FAPESP (Brazil) under the grant FAPESP #2021/06546-1. The authors acknowledge the Consortium des Moyens Technologiques Communs (CMTC) within the INP in Grenoble for the use of its facilities.

Appendix A. Supporting information

Supplementary data associated with this article can be found in the online version at doi:10.1016/j.corsci.2022.110607.

References

[1] B.D. Ratner, A.S. Hoffman, F.J. Schoen, J.E. Lemons, Biomaterials Science: An Introduction to Materials in Medicine, 2a, Elsevier Science, 2004. https://books.google.fr/books?id=9PMU1iYGe34C.
[2] C. Leinenbach, D. Eifler, Fatigue and cyclic deformation behaviour of surface-modified titanium alloys in simulated physiological media, Biomaterials 27 (2006) 1200–1208, https://doi.org/10.1016/j.biomaterials.2005.08.012.
[3] R. Bosco, E.R.U. Edreira, J.G.C. Wolke, S.C.G. Leeuwenburgh, J.J.J.P. van den Beucken, J.A. Jansen, Instructive coatings for biological guidance of bone implants, Surf. Coat. Technol. 233 (2013) 91–98, https://doi.org/10.1016/j.surfcoat.2013.02.039.
[4] R. Bosco, J.V. Van Den Beucken, S. Leeuwenburgh, J. Jansen, Surface engineering for bone implants: a trend from passive to active surfaces, Coatings 2 (2012) 95–119, https://doi.org/10.3390/coatings2030095.
[5] M. Geetha, A.K. Singh, R. Asokamani, A.K. Gogia, Ti based biomaterials, the ultimate choice for orthopaedic implants – a review, Prog. Mater. Sci. 54 (2009) 397–425, https://doi.org/10.1016/j.pmatsci.2008.06.004.
[6] Q. Chen, G.A. Thouas, Metallic implant biomaterials, Mater. Sci. Eng. R. Rep. 87 (2015) 1–57, https://doi.org/10.1016/j.mser.2014.10.001.
[7] M. Long, H.J. Rack, Titanium alloys in total joint replacement—a materials science perspective, Biomaterials 19 (1998) 1621–1639, https://doi.org/10.1016/S0142-9612(97)00146-4.
[8] P.G. Laing, A.B. Ferguson Jr., E.S. Hodge, Tissue reaction in rabbit muscle exposed to metallic implants, J. Biomed. Mater. Res 1 (1967) 135–149, https://doi.org/10.1002/jbm.820010113.
[9] M. Niinomi, Recent metallic materials for biomedical applications, Metall. Mater. Trans. A 33A (2002) 477–486.
[10] H. Schlicht, E. Wintermantel, Single-use instrumente in der endoskopischen Gastroenterologie, in: E. Wintermantel, S.-W. Ha (Eds.), Medizintechnik, Life Sci. Eng., Springer Berlin Heidelberg, Berlin, Heidelberg, 2009, pp. 1189–1214, https://doi.org/10.1007/978-3-540-93936-8_51.
[11] A.J. Engler, S. Sen, H.L. Sweeney, D.E. Discher, Matrix elasticity directs stem cell lineage specification, Cell 126 (2006) 677–689, https://doi.org/10.1016/j.cell.2006.06.044.
[12] G.C. Reilly, A.J. Engler, Intrinsic extracellular matrix properties regulate stem cell differentiation, J. Biomech. 43 (2010) 55–62, https://doi.org/10.1016/j.jbiomech.2009.09.009.
[13] S. Nag, R. Banerjee, H.L. Fraser, Microstructural evolution and strengthening mechanisms in Ti–Nb–Zr–Ta, Ti–Mo–Zr–Fe and Ti–15Mo biocompatible alloys, Mater. Sci. Eng. C. 25 (2005) 357–362, https://doi.org/10.1016/j.msec.2004.12.013.
[14] C. Lubov Donaghy, R. Mcfadden, S. Kelaini, L. Carson, A. Margariti, C. Chan, Creating an antibacterial surface on beta TNZT alloys for hip implant applications by laser nitriding, Opt. Laser Technol. 121 (2020), 105793, https://doi.org/10.1016/j.optlastec.2019.105793.
[15] X. Yang, C.R. Hutchinson, Corrosion-wear of β-Ti alloy TMZF (Ti-12Mo-6Zr-2Fe) in simulated body fluid, Acta Biomater. 42 (2016) 429–439, https://doi.org/10.1016/j.actbio.2016.07.008.
[16] S. Samuel, S. Nag, T.W. Scharf, R. Banerjee, Wear resistance of laser-deposited boride reinforced Ti-Nb–Zr–Ta alloy composites for orthopedic implants, Mater. Sci. Eng. C. 28 (2008) 414–420, https://doi.org/10.1016/j.msec.2007.04.029.
[17] M. Todai, T. Nagase, T. Hori, A. Matsugaki, A. Sekita, T. Nakano, Novel TiNbTaZrMo high-entropy alloys for metallic biomaterials, Scr. Mater. 129 (2017) 65–68, https://doi.org/10.1016/j.scriptamat.2016.10.028.
[18] D.B. Miracle, O.N. Senkov, A critical review of high entropy alloys and related concepts, Acta Mater. 122 (2017) 448–511, https://doi.org/10.1016/j.actamat.2016.08.081.
[19] J.-W. Yeh, S.-K. Chen, S.-J. Lin, J.-Y. Gan, T.-S. Chin, T.-T. Shun, C.-H. Tsau, S.-Y. Chang, Nanostructured high-entropy alloys with multiple principal elements: novel alloy design concepts and outcomes, Adv. Eng. Mater. 6 (2004) 299–303, https://doi.org/10.1002/adem.200300567.
[20] S. Guo, C.T. Liu, Phase stability in high entropy alloys: formation of solid-solution phase or amorphous phase, Prog. Nat. Sci. Mater. Int. 21 (2011) 433–446, https://doi.org/10.1016/S1002-0071(12)60080-X.
[21] B.S. Murty, J. Yeh, S. Ranganathan, - Phase selection in high-entropy alloys, in: High Entropy Alloy, 2014, pp. 37–56, https://doi.org/10.1016/B978-0-12-800251-3.00003-1.
[22] Q. Zhou, S. Sheikh, P. Ou, D. Chen, Q. Hu, S. Guo, Corrosion behavior of Hf0.5Nb0.5Ta0.5Ti1.5Zr refractory high-entropy in aqueous chloride solutions, Electrochem. Commun. 98 (2019) 63–68. https://doi.org/10.1016/j.elecom.2018.11.009.
[23] Y.F. Ye, Q. Wang, J. Lu, C.T. Liu, Y. Yang, High-entropy alloy: challenges and prospects, Mater. Today 19 (2016) 349–362, https://doi.org/10.1016/j.mattod.2015.11.026.
[24] W. Zhang, P.K. Liaw, Y. Zhang, Science and technology in high-entropy alloys, Sci. China Mater. 61 (2018) 2–22, https://doi.org/10.1007/s40843-017-9195-8.
[25] J.-W. Yeh, Physical Metallurgy of High-Entropy Alloys, JOM 67 (2015) 2254–2261, https://doi.org/10.1007/s11837-015-1583-5.

[26] R. Swalin, Thermodynamics of solids, 2nd Ed., Wiley-Interscience 1972–12-15, 1972.

[27] J.-W. Yeh, Alloy design strategies and future trends in high-entropy alloys, JOM 65 (2013) 1759–1771, https://doi.org/10.1007/s11837-013-0761-6.

[28] K.-Y. Tsai, M.-H. Tsai, J.-W. Yeh, Sluggish diffusion in Co–Cr–Fe–Mn–Ni high-entropy alloys, Acta Mater. 61 (2013) 4887–4897, https://doi.org/10.1016/j.actamat.2013.04.058.

[29] J.-W. Yeh, S.-Y. Chang, Y.-D. Hong, S.-K. Chen, S.-J. Lin, Anomalous decrease in X-ray diffraction intensities of Cu–Ni–Al–Co–Cr–Fe–Si alloy systems with multi-principal elements, Mater. Chem. Phys. 103 (2007) 41–46, https://doi.org/10.1016/j.matchemphys.2007.01.003.

[30] C.-Y. Hsu, J.-W. Yeh, S.-K. Chen, T.-T. Shun, Wear resistance and high-temperature compression strength of Fcc CuCoNiCrAl0.5Fe alloy with boron addition, Metall. Mater. Trans. A 35 (2004) 1465–1469, https://doi.org/10.1007/s11661-004-0254-x.

[31] J.W. Yeh, Y.L. Chen, S.J. Lin, S.K. Chen, High-Entropy Alloys – A New Era of Exploitation, in: Adv. Struct. Mater. III, Trans Tech Publications Ltd, 2007: pp. 1–9. https://doi.org/10.4028/www.scientific.net/MSF.560.1.

[32] W.F. Smith. Structure and Properties of Engineering Alloys, second ed., McGraw-Hill, New York, NY, 1993.

[33] B. Fultz, Vibrational thermodynamics of materials, Prog. Mater. Sci. 55 (2010) 247–352, https://doi.org/10.1016/j.pmatsci.2009.05.002.

[34] Y. Zhang, Y.J. Zhou, J.P. Lin, G.L. Chen, P.K. Liaw, Solid-Solution Phase Formation Rules for Multi-component Alloys, Adv. Eng. Mater. 10 (2008) 534–538, https://doi.org/10.1002/adem.200700240.

[35] X. Yang, Y. Zhang, Prediction of high-entropy stabilized solid-solution in multicomponent alloys, Mater. Chem. Phys. 132 (2012) 233–238, https://doi.org/10.1016/j.matchemphys.2011.11.021.

[36] A. Takeuchi, K. Amiya, T. Wada, K. Yubuta, W. Zhang, A. Makino, Entropies in alloy design for high-entropy and bulk glassy alloys, Entropy 15 (2013) 3810–3821, https://doi.org/10.3390/e15093810.

[37] Y.F. Ye, Q. Wang, J. Lu, C.T. Liu, Y. Yang, The generalized thermodynamic rule for phase selection in multicomponent alloys, Intermetallics 59 (2015) 75–80, https://doi.org/10.1016/j.intermet.2014.12.011.

[38] D.J.M. King, S.C. Middleburgh, A.G. McGregor, M.B. Cortie, Predicting the formation and stability of single phase high-entropy alloys, Acta Mater. 104 (2016) 172–179, https://doi.org/10.1016/j.actamat.2015.11.040.

[39] D. Miracle, B. Majumdar, K. Wertz, S. Gorsse, New strategies and tests to accelerate discovery and development of multi-principal element structural alloys, Scr. Mater. 127 (2017) 195–200, https://doi.org/10.1016/j.scriptamat.2016.08.001.

[40] D.B. Miracle, O.N. Senkov, A critical review of high entropy alloys and related concepts, Acta Mater. 122 (2017) 448–511, https://doi.org/10.1016/j.actamat.2016.08.081.

[41] W.-Y. Ching, S. San, J. Brechtl, R. Sakidja, M. Zhang, P.K. Liaw, Fundamental electronic structure and multiatomic bonding in 13 biocompatible high-entropy alloys, npj Comput. Mater. 6 (2020) 1–10, https://doi.org/10.1038/s41524-020-0321-x.

[42] P. Thomsen, C. Larsson, L.E. Ericson, L. Sennerby, J. Lausmaa, B. Kasemo, Structure of the interface between rabbit cortical bone and implants of gold, zirconium and titanium, J. Mater. Sci. Mater. Med 8 (1997) 653–665, https://doi.org/10.1023/A:1018579605426.

[43] H. Matsuno, A. Yokoyama, F. Watari, M. Uo, T. Kawasaki, Biocompatibility and osteogenesis of refractory metal implants, titanium, hafnium, niobium, tantalum and rhenium, Biomaterials 22 (2001) 1253–1262, https://doi.org/10.1016/S0142-9612(00)00275-1.

[44] E. Eisenbarth, D. Velten, M. Müller, R. Thull, J. Breme, Biocompatibility of beta-stabilizing elements of titanium alloys, Biomaterials 25 (2004) 5705–5713, https://doi.org/10.1016/j.biomaterials.2004.01.021.

[45] L. Saldaña, A. Méndez-Vilas, L. Jiang, M. Multigner, J.L. González-Carrasco, M. T. Pérez-Prado, M.L. González-Martín, L. Munuera, N. Vilaboa, In vitro biocompatibility of an ultrafine grained zirconium, Biomaterials 28 (2007) 4343–4354, https://doi.org/10.1016/j.biomaterials.2007.06.015.

[46] R.M. Hoerth, M.R. Katunar, A. Gomez Sanchez, J.C. Orellano, S.M. Ceré, W. Wagermaier, J. Ballarre, A comparative study of zirconium and titanium implants in rat: osseointegration and bone material quality., J. Mater. Sci. Mater. Med. 25 (2014) 411–422. https://doi.org/10.1007/s10856–013-5074–3.

[47] A.M. Ribeiro, T.H.S. Flores-Sahagun, R.C. Paredes, A perspective on molybdenum biocompatibility and antimicrobial activity for applications in implants, J. Mater. Sci. 51 (2016) 2806–2816, https://doi.org/10.1007/s10853-015-9664-y.

[48] J. Jayaraj, C. Thinaharan, S. Ningshen, C. Mallika, U. Kamachi Mudali, Corrosion behavior and surface film characterization of TaNbHfZrTi high entropy alloy in aggressive nitric acid medium, Intermetallics 89 (2017) 123–132, https://doi.org/10.1016/j.intermet.2017.06.002.

[49] Y. Shi, B. Yang, X. Xie, J. Brechtl, K.A. Dahmen, P.K. Liaw, Corrosion of Al xCoCrFeNi high-entropy alloys: Al-content and potential scan-rate dependent pitting behavior, Corros. Sci. 119 (2017) 33–45, https://doi.org/10.1016/j.corsci.2017.02.019.

[50] C.-M. Lin, H.-L. Tsai, Evolution of microstructure, hardness, and corrosion properties of high-entropy Al0.5CoCrFeNi alloy, Intermetallics. 19 (2011) 288–294. https://doi.org/https://doi.org/10.1016/j.intermet.2010.10.008.

[51] Y. Qiu, Z. Liu, D. Qu, Filtered bank based implementation for filtered OFDM, in: 2017 7th IEEE Int. Conf. Electron. Inf. Emerg. Commun., 2017: pp. 15–18. https://doi.org/10.1109/ICEIEC.2017.8076502.

[52] Y. Shi, B. Yang, P.K. Liaw, Corrosion-resistant high-entropy alloys: a review, Met. (Basel) 7 (2017) 1–18, https://doi.org/10.3390/met7020043.

[53] M.F. del Grosso, G. Bozzolo, H.O. Mosca, Determination of the transition to the high entropy regime for alloys of refractory elements, J. Alloy. Compd. 534 (2012) 25–31, https://doi.org/10.1016/j.jallcom.2012.04.053.

[54] Y.Y. Chen, T. Duval, U.D. Hung, J.W. Yeh, H.C. Shih, Microstructure and electrochemical properties of high entropy alloys—a comparison with type-304 stainless steel, Corros. Sci. 47 (2005) 2257–2279, https://doi.org/10.1016/j.corsci.2004.11.008.

[55] S.D. Cramer, J. Covino Bernard, S. Corrosion, Fundamentals, Testing, and Protection, ASM International, 2003, https://doi.org/10.31399/asm.hb.v13a.9781627081825.

[56] W. Yang, Y. Liu, S. Pang, P.K. Liaw, T. Zhang, Bio-corrosion behavior and in vitro biocompatibility of equimolar TiZrHfNbTa high-entropy alloy, Intermetallics 124 (2020), 106845, https://doi.org/10.1016/j.intermet.2020.106845.

[57] S. Guo, C. Ng, C.T. Liu, Anomalous solidification microstructures in Co-free AlxCrCuFeNi2 high-entropy alloys, J. Alloy. Compd. 557 (2013) 77–81, https://doi.org/10.1016/j.jallcom.2013.01.007.

[58] NIST X-ray Photoelectron Spectroscopy Database, NIST Standard Reference Database Number 20, National Institute of Standards and Technology, Gaithersburg MD, 20899 (2000), (n.d.). https://doi.org/10.18434/T4T88K.

[59] A. Carnot, I. Frateur, P. Marcus, B. Tribollet, Corrosion mechanisms of steel concrete moulds in the presence of a demoulding agent, J. Appl. Electrochem 32 (2002) 865–869, https://doi.org/10.1023/A:1020510506504.

[60] S. Chakri, P. David, I. Frateur, A. Galtayries, P. Marcus, E. Sutter, B. Tribollet, B., Vivier, V., Zanna, S., Effet de la composition chimique de la solution interstitielle de bétons jeunes sur la passivation d′un acier doux, Matériaux & Tech. 103 (2015) 209. https://doi.org/10.1051/mattech/2015016.

[61] L.L. De Sousa, V.P. Ricci, D.G. Prado, R.C. Apolinario, L.C. De Oliveira Vercik, E. C. Da Silva Rigo, M.C. Dos Santos Fernandes, N.A. Mariano, Titanium coating with hydroxyapatite and chitosan doped with silver nitrate, Mater. Res. 20 (2017) 863–868, https://doi.org/10.1590/1980-5373-mr-2017-0021.

[62] P. Chui, R. Jing, F. Zhang, J. Li, T. Feng, Mechanical properties and corrosion behavior of β-type Ti-Zr-Nb-Mo alloys for biomedical application, J. Alloy. Compd. 842 (2020), 155693, https://doi.org/10.1016/j.jallcom.2020.155693.

[63] M. Metikoš-Huković, A. Kwokal, J. Piljac, The influence of niobium and vanadium on passivity of titanium-based implants in physiological solution, Biomaterials 24 (2003) 3765–3775, https://doi.org/10.1016/S0142-9612(03)00252-7.

[64] S.Y. Yu, J.R. Scully, C.M. Vitus, Influence of niobium and zirconium alloying additions on the anodic dissolution behavior of activated titanium in {HCl} solutions, J. Electrochem. Soc. 148 (2001) B68, https://doi.org/10.1149/1.1337605.

[65] S.Y. Yu, J.R. Scully, Corrosion and passivity of Ti-13% Nb-13% Zr in comparison to other biomedical implant alloys, Corrosion 53 (1997) 965–976, https://doi.org/10.5006/1.3290281.

[66] D.O. Scanlon, G.W. Watson, D.J. Payne, G.R. Atkinson, R.G. Egdell, D.S.L. Law, Theoretical and experimental study of the electronic structures of MoO3 and MoO2, J. Phys. Chem. C 114 (2010) 4636–4645, https://doi.org/10.1021/jp9093172.

[67] O.Y. Khyzhun, V.L. Bekenev, Y.M. Solonin, Electronic structure of face-centred cubic MoO2: A comparative study by the full potential linearized augmented plane wave method, X-ray emission spectroscopy and X-ray photoelectron spectroscopy, J. Alloy. Compd. 459 (2008) 22–28, https://doi.org/10.1016/j.jallcom.2007.04.281.

[68] I.A. de Castro, R.S. Datta, J.Z. Ou, A. Castellanos-Gomez, S. Sriram, T. Daeneke, K. Kalantar-Zadeh, Molybdenum oxides – from fundamentals to functionality, Adv. Mater. 29 (2017) 1–31, https://doi.org/10.1002/adma.201701619.

[69] K.L. Chao, H.Y. Liao, J.J. Shyue, S.S. Lian, Corrosion behavior of high nitrogen nickel-free Fe-16Cr-Mn-Mo-N stainless steels, Metall. Mater. Trans. B Process. Metall. Mater. Process. Sci. 45 (2014) 381–391, https://doi.org/10.1007/s11663-013-9891-z.

[70] V.S. Saji, C.W. Lee, Molybdenum, molybdenum oxides, and their electrochemistry, 1146–61, ChemSusChem 5 (2012), https://doi.org/10.1002/cssc.201100660.

[71] W.A. Badawy, F.M. Al-Kharafi, Corrosion and passivation behaviors of molybdenum in aqueous solutions of different pH, Electrochim. Acta 44 (1998) 693–702, https://doi.org/10.1016/S0013-4686(98)00180-7.

[72] L. De Rosa, C.R. Tomachuk, J. Springer, D.B. Mitton, S. Saiello, F. Bellucci, The wet corrosion of molybdenum thin film –. part I: behavior at 25 ° C, Mater. Corros. 55 (2004) 602–609, https://doi.org/10.1002/maco.200303785.

[73] T.J. Mesquita, E. Chauveau, M. Mantel, R.P. Nogueira, A XPS study of the Mo effect on passivation behaviors for highly controlled stainless steels in neutral and alkaline conditions, Appl. Surf. Sci. 270 (2013) 90–97, https://doi.org/10.1016/j.apsusc.2012.12.118.

[74] L. Staišiūnas, K. Leinartas, E. Juzeliūnas, D. Bučinskienė, A. Grigucevičienė, P. Kalinauskas, A. Selskis, S. Stanionytė, Anticorrosion performance of hafnium oxide ultrathin films on AZ31 magnesium alloy, Surf. Coat. Technol. 397 (2020), https://doi.org/10.1016/j.surfcoat.2020.126046.

[75] M. Pourbaix, Atlas of electrochemical equilibria in aqueous solution, NACE 307 (1974). 〈https://ci.nii.ac.jp/naid/10011714604/en/〉.

[76] J.A. Field, A. Luna-Velasco, S.A. Boitano, F. Shadman, B.D. Ratner, C. Barnes, R. Sierra-Alvarez, Cytotoxicity and physicochemical properties of hafnium oxide nanoparticles, Chemosphere 84 (2011) 1401–1407, https://doi.org/10.1016/j.chemosphere.2011.04.067.

[77] D. Zhang, Z. Qi, B. Wei, Z. Wang, Low temperature thermal oxidation towards hafnium-coated magnesium alloy for biomedical application, Mater. Lett. 190 (2017) 181–184, https://doi.org/10.1016/j.matlet.2017.01.009.

[78] J. Rituerto Sin, A. Neville, N. Emami, Corrosion and tribocorrosion of hafnium in simulated body fluids, J. Biomed. Mater. Res. Part B Appl. Biomater. 102 (2014) 1157–1164, https://doi.org/10.1002/jbm.b.33097.

[79] Y.H. Chen, W.S. Chuang, J.C. Huang, X. Wang, H.S. Chou, Y.J. Lai, P.H. Lin, On the bio-corrosion and biocompatibility of TiTaNb medium entropy alloy films, Appl. Surf. Sci. 508 (2020), 145307, https://doi.org/10.1016/j.apsusc.2020.145307.

[80] A.H. Hussein, M.A.-H. Gepreel, M.K. Gouda, A.M. Hefnawy, S.H. Kandil, Biocompatibility of new Ti–Nb–Ta base alloys, Mater. Sci. Eng. C. 61 (2016) 574–578, https://doi.org/10.1016/j.msec.2015.12.071.

[81] D.B. Wei, X.H. Chen, P.Z. Zhang, F. Ding, F.K. Li, Z.J. Yao, Plasma surface tantalum alloying on titanium and its corrosion behavior in sulfuric acid and hydrochloric acid, Appl. Surf. Sci. 441 (2018) 448–457, https://doi.org/10.1016/j.apsusc.2018.02.058.

[82] P. Kumar, N. Duraipandy, K. Manikantan Syamala, N. Rajendran, Antibacterial effects, biocompatibility and electrochemical behavior of zinc incorporated niobium oxide coating on 316L SS for biomedical applications, Appl. Surf. Sci. 427 (2018) 1166–1181, https://doi.org/10.1016/j.apsusc.2017.08.221.

[83] A.W.E. Hodgson, Y. Mueller, D. Forster, S. Virtanen, Electrochemical characterisation of passive films on Ti alloys under simulated biological conditions, Electrochim. Acta 47 (2002) 1913–1923, https://doi.org/10.1016/S0013-4686(02)00029-4.

[84] H. Luo, Z. Li, A.M. Mingers, D. Raabe, Corrosion behavior of an equiatomic CoCrFeMnNi high-entropy alloy compared with 304 stainless steel in sulfuric acid solution, Corros. Sci. 134 (2018) 131–139, https://doi.org/10.1016/j.corsci.2018.02.031.

[85] D.D. Macdonald, M.C.H. Mckubre, J.O.M. Bockris, B.E. Conway, R.E. White, Mod. Asp. Electrochem. vol. 14 (1982).

[86] P. Ćordoba-Torres, N.T.C. Oliveira, C. Bolfarini, V. Roche, R.P. Nogueira, Electrochemical impedance analysis of TiO2 nanotube porous layers based on an alternative representation of impedance data, J. Electroanal. Chem. 737 (2015) 54–64, https://doi.org/10.1016/j.jelechem.2014.06.034.

[87] X.L. Zhang, Z.H. Jiang, Z.P. Yao, Z.D. Wu, Electrochemical study of growth behaviour of plasma electrolytic oxidation coating on Ti6Al4V: effects of the additive, Corros. Sci. 52 (2010) 3465–3473, https://doi.org/10.1016/j.corsci.2010.06.017.

[88] C. Delgado-Alvarado, P.A. Sundaram, Corrosion evaluation of Ti–48Al–2Cr–2Nb (at%) in Ringer's solution, Acta Biomater. 2 (2006) 701–708, https://doi.org/10.1016/j.actbio.2006.05.012.

[89] R.M. Souto, M.M. Laz, R.L. Reis, Degradation characteristics of hydroxyapatite coatings on orthopaedic TiAlV in simulated physiological media investigated by electrochemical impedance spectroscopy, Biomaterials 24 (2003) 4213–4221, https://doi.org/10.1016/S0142-9612(03)00362-4.

[90] A.K. Shukla, R. Balasubramaniam, Effect of surface treatment on electrochemical behavior of CP Ti, Ti–6Al–4V and Ti–13Nb–13Zr alloys in simulated human body fluid, Corros. Sci. 48 (2006) 1696–1720, https://doi.org/10.1016/j.corsci.2005.06.003.

[91] V. Raman, S. Tamilselvi, N. Rajendran, Electrochemical impedance spectroscopic characterization of titanium during alkali treatment and apatite growth in simulated body fluid, Electrochim. Acta 52 (2007) 7418–7424, https://doi.org/10.1016/j.electacta.2007.06.040.

[92] S. Tamilselvi, V. Raman, N. Rajendran, Corrosion behaviour of Ti–6Al–7Nb and Ti–6Al–4V ELI alloys in the simulated body fluid solution by electrochemical impedance spectroscopy, Electrochim. Acta 52 (2006) 839–846, https://doi.org/10.1016/j.electacta.2006.06.018.

[93] B. Tribollet, V. Vivier, M.E. Orazem EIS Technique in Passivity Studies: Determination of the Dielectric Properties of Passive Films, Ed. Klaus Wandelt, Encyclopedia of Interfacial Chemistry, Elsevier, 2018, Pages 93–107, ISBN 9780128098943, https://doi.org/10.1016/B978–0-12–409547-2.13817-X.

[94] M. Benoit, C. Bataillon, B. Gwinner, F. Miserque, M.E. Orazem, C.M. Śanchez-Śanchez, V. B.Tribollet, Viviera, Comparison of different methods for measuring the passive film thickness on metals, Electrochim. Acta 201 (2016) 340–347, https://doi.org/10.1016/j.electacta.2015.12.173.

[95] C.H. Hsu, F. Mansfield, Technical note: concerning the conversion of the constant phase element parameter y0 into a capacitance, Corrosion 57 (2001) 747–748, https://doi.org/10.5006/1.3280607.

[96] M.E. Orazem, B. Tribollett, Electrochemical impedance spectroscopy. Agric. Food Electroanal., second edition, 2015, pp. 381–419, https://doi.org/10.1002/9781118684030.ch14.

[97] H. Liu, J. Yang, X. Zhao, Y. Sheng, W. Li, C.L. Chang, Q. Zhang, Z. Yu, X. Wang, Microstructure, mechanical properties and corrosion behaviors of biomedical Ti-Zr-Mo-xMn alloys for dental application, Corros. Sci. 161 (2019) 2–15, https://doi. org/10.1016/j.corsci.2019.108195.

[98] S.L. De Assis, S. Wolynec, I. Costa, Corrosion characterization of titanium alloys by electrochemical techniques, Electrochim. Acta 51 (2006) 1815–1819, https://doi. org/10.1016/j.electacta.2005.02.121.

[99] D.Q. Martins, W.R. Osório, M.E.P. Souza, R. Caram, A. Garcia, Effects of Zr content on microstructure and corrosion resistance of Ti-30Nb-Zr casting alloys for biomedical applications, Electrochim. Acta 53 (2008) 2809–2817, https://doi.org/10.1016/j.electacta.2007.10.060.

[100] G.J. Brug, A.L.G. van den Eeden, M. Sluyters-Rehbach, J.H. Sluyters, The analysis of electrode impedances complicated by the presence of a constant phase element, J. Electroanal. Chem. Interfacial Electrochem 176 (1984) 275–295, https://doi.org/10.1016/S0022-0728(84)80324-1.

[101] J.Y. Kim, D.-W. Kim, H.S. Jung, K.S. Hong, Influence of anatase–rutile phase transformation on dielectric properties of sol–gel derived TiO2 thin films, Jpn. J. Appl. Phys. 44 (2005) 6148, https://doi.org/10.1143/JJAP.44.6148.

[102] J. Robertson, High dielectric constant oxides, Eur. Phys. J. Appl. Phys. 28 (2004) 265–291, https://doi.org/10.1051/epjap:2004206.

[103] Woojin Jeon, Recent advances in the understanding of high-k dielectric materials deposited by atomic layer deposition for dynamic random-access memory capacitor applications, J. Mater. Res. 35 (2020) 775–794, https://doi.org/10.1557/jmr.2019.335.

[104] J.Y. Kim, H.S. Jung, J.H. No, et al., Influence of anatase-rutile phase transformation on dielectric properties of sol-gel derived TiO2 thin films, J. Electroceram 16 (2006) 447–451, https://doi.org/10.1007/s10832-006-9895-z.

[105] R. Brian, Strohmeier. An ESCA method for determining the oxide thickness on aluminum alloys, Surf. Interface Analyisis 15 (1990) 51–56, https://doi.org/10.1002/sia.740150109.

[106] Cumpson. The Thickogram: a method for easy film thickness measurement in XPS. Surface and Interface Analysis 29, 403–406 (2000). https://doi.org/10.1002/1096–9918(200006)29:63.0.CO;2–

[107] Roger W.. Welker, Chapter 4 - Size Analysis and Identification of Particles. Rajiv Kohli, K.L. Mittal (Eds), in: Developments in Surface Contamination and Cleaning. William Andrew Publishing, 2012, Pages 179–213, ISBN 9781437778830, https://doi.org/10.1016/B978–1-4377–7883-0.00004–3.